Geomech. Geophys. Geo-energ. Geo-resour. (2023) 9:107
https://doi.org/10.1007/s40948-023-00634-z

CORRESPONDENCE

A micromechanical investigation of diagenetically-induced changes to the anisotropic elastic properties of calcareous mudstones

Samuel P. Graham · Andrew C. Aplin · Mohamed Rouainia · Mark T. Ireland · Peter J. Armitage

Received: 29 September 2022 / Accepted: 27 June 2023

Abstract Microscale diagenetic changes that occur during burial exert a profound influence on the elastic and mechanical properties of sediments—but are poorly quantified. The focus here is on how diagenesis influences the elastic properties of carbonate-rich mudstones, which are subject to a wide range of physical and chemical changes. Nanoindentation data for gas-window (180 °C) Eagle Ford formation samples give intrinsic indentation moduli of the clay-sized calcite matrix of $M = 40$–50 GPa, which contrasts with $M = 60$–77 GPa for diagenetic calcite fills of foraminifera tests, closer to values for highly crystalline calcite. The matrix calcite is weakly anisotropic. Inverse analysis of immature (< 70 °C) organic-rich chalks gives much lower intrinsic indentation moduli for biogenic calcite, between 17 and 30 GPa; the calcite is also more anisotropic, with values of $M_1/M_3 \sim 1.3$. Diagenesis, which includes recrystallisation and pore-filling cementation, results in calcite becoming elastically stiffer and behaving in an increasingly isotropic manner, in agreement with grain scale studies using atomic force microscopy. The results demonstrate that nanoindentation can resolve diagenetic contributions to the mechanical response of mudstones, and suggest intrinsic structural changes to calcite, in addition to diagenetic cementation, need to be accounted for in rock-physics models of mud-rich sediments.

Article highlights

- Nanoindentation experiments are shown to be capable of resolving diagenetically related differences in the elastic behaviour of mudstone microstructure.
- A micromechanical conceptual model for organic-rich chalks is presented. This is implemented in a mean-field homogenisation numerical framework to explore the elastic anisotropy of fine grained carbonates during early burial.

Present Address:
S. P. Graham (✉) · M. Rouainia (✉)
School of Engineering, Newcastle University, Newcastle upon Tyne NE1 7RU, UK
e-mail: sam.graham@ed.ac.uk

M. Rouainia
e-mail: mohamed.rouainia@ncl.ac.uk

S. P. Graham
School of Geosciences, Grant Institute, The King's Buildings, University of Edinburgh, Edinburgh EH9 3FE, UK

A. C. Aplin
Department of Earth Sciences, Durham University, Durham DH1 3LE, UK

M. T. Ireland
School of Natural and Environmental Sciences, Newcastle University, Newcastle upon Tyne NE1 7RU, UK

P. J. Armitage
BP, Sunbury on Thames TW16 7LN, UK

Published online: 26 August 2023

- Nanoindentation experiments and micromechanical models are combinded to explore the evolution of anisotropy during burial of fine-grained calcareous sediments.
- A discussion of potential improvements in the interpretation of traditional velocity-porosity plots offered by micromechanical experimental and modelling approaches is offered.

Keywords Calcite · Chalk · Limestone · Nanoindentation · Diagenesis · Homogenisation · Micromechanics · Petrophysics

1 Introduction

Well-constrained elastic properties are critical parameters both for modelling the mechanical behaviour of sedimentary rocks and for the accurate interpretation of seismic velocity data. Nanoindentation, coupled with multiscale micromechanical models has become an increasingly popular tool to understand the mechanical properties of mudstones (Sondergeld and Rai 2022), with its application particularly focused on refining the elastic properties of clay-mineral and organic matter assemblages (Bobko and Ulm 2008; Abedi et al. 2016). From deposition to maximum burial, mechanical properties are fundamentally altered as a result of diagenesis: physical and chemical changes including compaction and alterations to the composition and/or microstructure of the primary sediment (Obradors-Prats et al. 2019). Microscale diagenetic changes exert a profound influence on the macromechanical properties of sediments and thus, for example, the development of fractures, faults and geological structures Laubach et al. (2009, 2010).

An overarching issue is to understand and predict the mineralogical and diagenetic controls that underpin changes in the elastic and mechanical properties of sedimentary rocks. Of particular interest are the properties of mudstones, given their volumetric dominance in basins and their highly varied mineralogical composition. In this paper, our specific focus is on carbonate-rich mudstones, which are subject to a wide range of physical and chemical changes during burial diagenesis.

Diagenetic processes acting on carbonate-rich mudstones include both mechanical and chemical compaction, pressure solution and stylotisation, recrystallisation, and both grain-contact and pore-filling cementation (Scholle 1977; Fabricius 2003). These mechanisms result in a wide range of microstructures and porosity types (Røgen et al. 2005; Fabricius et al. 2007; Brigaud et al. 2010; Regnet et al. 2015) that have only been partly explored, for example through the relationship between P- (or S-) wave velocity and porosity in chalk (e.g Fabricius 2007, Brigaud et al. 2010).

Mechanical interpretations of core-scale petrophysical data have commonly assumed that the elastic properties of non-clay mineral phases are tightly constrained and the same as those measured on highly crystalline materials (e.g. Ortega et al. 2007). For carbonates, this is not the case. Graham et al. (2021) showed that the Young's modulus for biogenic calcite in calcareous mudstone was significantly lower than that measured on highly crystalline calcite ("Iceland Spar"). Similarly, Røgen et al. (2005) found that for North-Sea chalks, zero-porosity elastic constants do not agree well with values based on measurements of highly crystalline calcite. Fabricius et al. (2007) noted different trends for the evolution of the Biot coefficient, α, as a function of porosity between the Tor formation and the Ekofisk formation (both North Sea chalks); these cannot be explained by a single set of elastic properties for calcite. The coefficient α is related to the relative stiffnesses of pores and framework (Zimmerman 2000; Fabricius et al. 2007). Whilst, in general, α decreases with decreasing porosity as pores are filled with carbonate cement Fabricius et al. (2007), it is not necessarily the case that the more macrocrystalline cement is elastically identical to the microcrystalline matrix; a more nuanced interpretation of the relationship between mechanical properties and the interplay of mechanical and chemical diagenesis is required for carbonate-rich mudstones.

Given the practical difficulties of obtaining high quality mechanical properties of mudstones in core-scale laboratory tests, micromechanical workflows have become an increasingly popular way of investigating both the elastic and creep properties of mudstones. Furthermore, micromechanical approaches have the advantage of measuring properties at the scale of the individual mineral building blocks. Both atomic force microscopy (AFM) and nanoindentation tests provide small length-scale mechanical

characterisation of material constituents, including clay minerals and organic matter (Eliyahu et al. 2015; Emmanuel et al. 2016; Goodarzi et al. 2017; Fender et al. 2020a, b; Graham et al. 2021). The advantage of small-scale experimental techniques allows direct measurements of mechanical properties at length scales comparable to the grain scale processes governing them. This contrasts with triaxial experiments where the experiment takes place on length scales several orders of magnitude above that of the grain. This can lead to only very generic relationships between composition and mechanical response, and uncertainty in the underlying, microstructural causative mechanism (Rybacki et al. 2017; Herrmann et al. 2018). With a mechanical measurements linked to the grain scale, these data can then be integrated into mean-field homogenisation models to predict the elastic behaviour of the bulk rock composite material, which can be strongly controlled by the grain scale properties. Several studies have demonstrated the ability of grain scale data combined with mean-field homogenisation tools, to predict the mechanical results of core scale tests (Ortega et al. 2007; Goodarzi et al. 2016, 2017; Li et al. 2019; Charlton et al. 2021), with Guéry et al. (2010) looking at multiple intervals in a borehole, or to back-calculate the mechanical properties of mechanical components such as clay minerals or organic matter that are otherwise poorly constrained (Ortega et al. 2007; Abedi et al. 2016). Nevertheless, there are limitations in the use of homogenisation models in that (a) they usually assume a single generalised microstructure (Ulm et al. 2005) and (b) the elastic properties of the non-clay mineral phases are well known and can be taken from the literature (e.g. Mavko et al. 2009). Experimental results (Graham et al. 2021), and modelling work (Graham and Rouainia 2021; Graham et al. 2022) suggest this may not be the case, particularly for calcareous mudstones.

Mean-field homogenisation models such as the Self-Consistent or Mori–Tanaka schemes (Hill 1965; Mori and Tanaka 1973) do not explicitly incorporate diagenetic factors in their mathematical formulation. Mashhadian et al. (2018a) and Dubey et al. (2019) have attempted to accommodate pore-filling cements through an interfacial transition zone, but this was treated as a calibration variable and was not experimentally verified. Fabricius (2003) proposed a method of incorporating cementation into a mechanical model for chalk using a combination of a modified Hashin-Shtrikman bound and Reuss bound to describe the progressive increase in load-bearing material as cement precipitates from pore fluid. However, this model assumed equivalent elastic properties for the cement and matrix. There is the need to use micromechanically appropriate elastic properties of primary and diagenetic phases in order to capture geological reality and enhance the predictive ability of mechanical models (e.g. Charlton et al. 2021). Combining micromechanical experimental techniques with mean-field homogenisation models may provide a way of incorporating important diagenetic detail into mechanical models of fine-grained sediments. Experimentally, we seek to extend the use of nanoindentation in mudstone geomechanics beyond its "traditional" geomechanics role in the characterisation of the mechanical behaviour of clay minerals. We seek to exploit the match of experimental and material length scales to investigate fundamental causative links between geological processes manifested in microstructure, and their consequences in terms of rock deformation.

The aim of this paper is to investigate the micromechanical consequences of diagenesis. We provide new nanoindentation data for Eagle Ford formation mudstones in the gas window (buried to > 180 °C), interpreted in terms of microstructures characterised using optical and scanning electron microscopy. A calcareous matrix of calcite mud and coccolith debris is common throughout the Eagle Ford sequence (Alnahwi et al. 2018). In gas-mature samples, cement fills to foraminifera are common, as well as domains where primary calcite has recrystallized (Driskill et al. 2012; Gaiani 2020). Significant organic matter porosity is generated (Pommer and Milliken 2015), although interparticle porosity is still maintained, although reduced compared to less mature examples (Gaiani 2020). Samples were specifically chosen to measure the mechanical properties of both the fine-grained calcareous matrix and the full range of diagenetic products. These results are compared to nanoindentation data from low maturity (< 90 °C) outcrop samples reported by Mashhadian et al. (2018b).

Additionally, to constrain the elastic properties of calcite in low maturity, fine-grained carbonates, we present inverse micromechanical modelling of literature data on thermally-immature, shallowly buried

organic-rich chalks (Gordin et al. 2016; Shitrit et al. 2019) in order to predict the nanoindentation behaviour of calcite for these samples. These datasets allow us to develop some hypotheses regarding the elastic properties of calcite in fine-grained sediments as a function of burial diagenesis, as well as presenting some predictions from which future micromechanical studies of calcareous mudstones can be benchmarked. These benchmarks incorporate mechanical diagenetic contributions within a micromechanics framework. Our results will provide a micromechanically informed dataset for incorporating calcite into mean-field homogenisation models as a function of diagenetic state.

2 Micromechanical methodology

To characterise the mechanical building blocks of samples of Eagle Ford mudstone, we use low-load nanoindentation grids. The technique is well established in materials research (Oliver and Pharr 1992), so only our protocols are given here. For micromechanical modelling, we use the Self-Consistent and Mori–Tanaka models (Hill 1965; Mori and Tanaka 1973) since these are capable of accounting for granular and matrix-inclusion microstructures seen in mudstones and have a wide applicability in capturing a range of multi-scale geological microstructures when used in combination (Charlton et al. 2021; Graham et al. 2022). The experimental procedures and micromechanical schemes are outlined in the following sections.

2.1 Nanoindentation

Three samples from the Eagle Ford formation are considered (gas window, $R_0 > 2\%$). The samples used in this study complement samples from the same formation presented in Graham et al. (2021), which only contained clay-sized calcite in the matrix, and were poor in foraminifera content. In contrast, the samples in the present study contain an abundance of large foraminifera tests filled completely with calcite cement. This makes these good samples to be used to assess the differences in mechanical behaviour between cements and the calcareous matrix.

A standard grid-indentation approach was taken to characterise the mechanical components based on a total of 400 indents per sample. Two core intervals, TS2 and TS4 (which are taken from a wider suite of seven samples), are considered with TS2 being tested in both perpendicular and parallel orientations, giving a total of three samples. Two samples received indents split across four, randomly positioned, subgrids of 100 indentations (10×10), consistent with the procedure used in Graham et al. (2021). The third sample was indented in a single indentation grid (20×20). This was done to provide a to provide a direct comparison with samples examined by Mashhadian et al. (2018b), who use a single grid approach. An indent spacing of 5 μm was used consistently throughout all tests. Load-controlled testing with a maximum force, P_{max}, of 5 mN was applied using a NanoTest Vantage instrument (MicroMaterials, Wrexham UK). Analysis of indentation curves was carried out according to the standard approach of Oliver and Pharr (1992), where the experimental indentation modulus M^{Exp} is given as

$$M^{Exp} = \frac{2\beta\sqrt{\pi}}{\sqrt{A_c}} S_{max} \tag{1a}$$

where A_c is the contact area between the indenter and sample, S_{max} is the gradient of the experimental unloading line at peak load, and $\beta = 1.034$ is a geometric factor. If M^{Exp} is obtained on an isotropic material, it can be written in terms of elastic constants as follows.

$$M^{ISO} = \frac{E}{1-\nu^2} \equiv \frac{C_{11}^2 - C_{12}^2}{C_{11}} \tag{1b}$$

where E is the Young's modulus and ν is Poisson's ratio. For transversely isotropic materials, the indentation moduli parallel and perpendicular to the material symmetry axes are given by Delafargue and Ulm (2004):

$$M_1 = \sqrt{\frac{C_{11}^2 - C_{12}^2}{C_{11}} \sqrt{\frac{C_{11}}{C_{33}}} M_3} \tag{1c}$$

$$M_3 = 2\sqrt{\frac{C_{11}C_{33} - C_{13}^2}{C_{11}}\left(\frac{1}{C_{44}} + \frac{2}{\sqrt{C_{13}C_{33}} + C_{33}}\right)^{-1}} \tag{1d}$$

where C_{ij} are components of the elastic stiffness tensor for the material. The low indentation loads employed in this study mean that it is appropriate to use Eq. 1a in analysing raw indentation curves, making an assumption of local isotropy. It should be noted that C_{ij} cannot be obtained directly from a single indentation test. Rather Eqs. 1b, 1c & 1d are presented in terms of components C_{ij} to facilitate the assessment of the inverse modelling results presented in Sect. 4, where we down-scale from core scale tests, and obtain values for C_{ij} from numerical models. These values are then used in Sect. 5 where we undertake some theoretical predictions of expected indentation responses based on earlier micromechanical experimental and modelling results.

2.2 Mean-field homogensiation

Mean-field homogenisation allows for the prediction of the elastic constants of a composite material from its constituents, assuming basic information about its porous microstructure. This paper employs two common techniques, namely the Self-Consistent and Mori–Tanaka methods (Hill 1965; Mori and Tanaka 1973). Their mathematical formulations are given below.

2.2.1 Self-consistent scheme

The Self-Consistent (SC) scheme approximates granular material with a critical porosity, the so-called percolation threshold (0.5 for spherical particles). Porosities above the percolation threshold correspond to particles no longer in contact with one another and a material with zero stiffness. The homogenized stiffness tensor, $\mathbb{C}^{\text{Hom}}$, for a composite of N phases can be written as:

$$\mathbb{C}^{\text{Hom}} = \sum_{i=1}^{N} f_i \mathbb{C}_i : \mathbb{A}_i^{\text{SC}} \tag{2a}$$

where f_i is the volume fraction, $\mathbb{C}_i$ is the stiffness tensor and $\mathbb{A}_i^{\text{SC}}$ is the strain localization tensor, which acts to map macroscopic strains on the composite material to the local strains in the grain, of the ith phase given by:

$$\mathbb{A}^{\text{SC}} = \left[\mathbb{I} + \mathbb{P}_i^{\text{Hom}} : (\mathbb{C}_i - \mathbb{C}^{\text{Hom}})\right]^{-1} \tag{2b}$$

where $\mathbb{I}$ is the fourth-order identity tensor and $\mathbb{P}_i^{\text{Hom}}$ is the Hill tensor, which accounts for the mechanical interaction between each mechanical phase and the composite. For the particular case of the isotropic indentation modulus, M^{ISO} scales with porosity under the SC method as follows:

$$\frac{M_{\text{SC}}^{\text{ISO}}}{m_s} = \begin{cases} 1 - 2\phi & \phi < 0.5 \\ 0 & \phi > 0.5 \end{cases} \tag{2c}$$

where m_s is the indentation modulus of the solid material at zero porosity, ϕ.

2.2.2 Mori–Tanaka Scheme

The Mori–Tanaka scheme is used to describe foam-like microstructures, which have a well-defined and continuous background phase into which pore space (or other solid phases) is added. Consequently, there is no percolation threshold, allowing this model to be applied over all possible porosities. The homogenized stiffness tensor, $\mathbb{C}^{\text{Hom}}$, for a composite of N phases can be written as:

$$\mathbb{C}^{\text{Hom}} = \mathbb{C}_0 + \sum_{i=1}^{N} f_i : (\mathbb{C}_i - \mathbb{C}_0) : \mathbb{A}_i^{\text{MT}} \tag{3a}$$

with the strain localisation tensor given as:

$$\mathbb{A}^{\text{MT}} = \left[\mathbb{I} + \mathbb{P}_i^0 : (\mathbb{C}_i - \mathbb{C}_0)\right]^{-1} \times \left[\sum_{i=1}^{N} f_i : [\mathbb{I} + \mathbb{P}_i^0 : (\mathbb{C}_i - \mathbb{C}_0)]^{-1}\right]^{-1} \tag{3b}$$

where $\mathbb{C}_0$ is the stiffness tensor for the background matrix phase, and $\mathbb{P}_i^0$ is Hill's tensor describing the interactions between the ith material phase and the background phase. In both Eqs. 2b and 3b, $\mathbb{P}$ is a function of particle geometry, and the elastic symmetry of the background material. For a background material with transversely isotropic symmetry, the components P_{ij} are given by Hellmich et al. (2004).

The indentation modulus scales with porosity under a MT model according to:

$$\frac{M_{\mathrm{MT}}^{\mathrm{ISO}}}{m_s} = \frac{1-\phi}{1+\phi} \tag{3c}$$

Figure 1 illustrates the evolution of the isotropic indentation modulus under both models according to Eqs. 3c and 2c, showing the influence of microstructure on measurement.

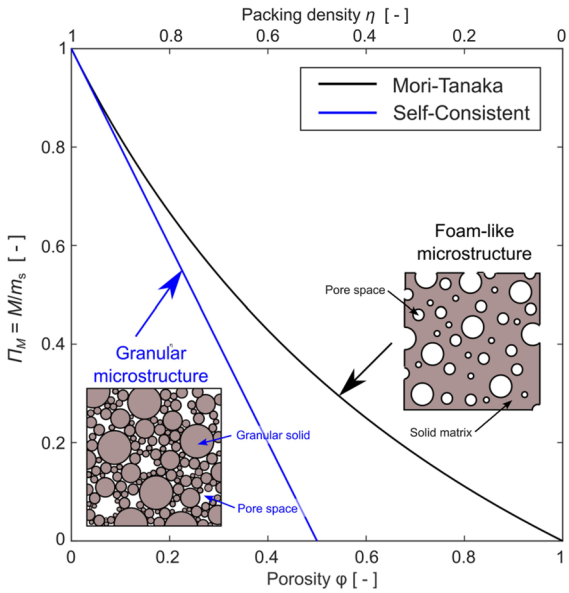

Fig. 1 Normalised effective indentation modulus for a dry porous material as a function of porosity for SC and MT models calculated according to Eqns. 2c and 3c. The normalised indentation moduli under the MT scheme are systematically higher than those predicted under the SC scheme over all porosities. This is due to the SC scheme being governed by a percolation threshold (i.e. a critical porosity, ϕ_{crit}); for $\phi > \phi_{\mathrm{crit}}$ no particles are in physical contact. The MT scheme employs a background phase that is continuous over all porosities

3 Eagle Ford samples

In this section we provide nanoindentation results from this formation further to those presented in Graham et al. (2021), but here with a focus on the link between elastic properties and microstructure. We use samples of mudstone from the Eagle Ford formation (TX, USA). Both samples TS2 and TS4 were analysed microstructurally using optical microscopy, and scanning electron microscopy. Composition was characterised by X-ray diffraction spectroscopy and porosity by mercury intrusion. A compositional summary is presented in Table 1.

3.1 Microstructural observations

Sample TS2: Calcite is present in two main forms—i) as the fill to foraminifera tests, and ii) as micron-sized calcite in the matrix comprising micritic mud, and disarticulated coccolith plates (Fig. 2). From the optical microscope study, it was seen that the calcite in the foraminifera tests displays uniform extinction under crossed-polarised light. This implies that the fills can be considered a mechanically continuous component, rather than comprising micritic mud. Sample porosity is largely confined to the calcareous matrix. Quartz is present as small, subhedral grains $< 10\ \mu$m in size, interspersed throughout the matrix. Quartz is again present as small grains up to 10 μm in size within the calcareous matrix. The feldspar grains are much larger upto 30 μm in size.

Sample TS4: The microstructure of TS4 (Fig. 3) is similar to that of TS2. Under the optical microscope, calcite filled forams sit within an optically opaque matrix. SEM imaging shows that this matrix is compositionally similar to TS2. The calcite fills to the foraminifera tests also display uniform extinction

Table 1 Summary of sample names, indentation directions, indentation grid arrangements and summary compositional and porosity information

Sample	Direction	Indent grid	Mineralogy (vol%)			Porosity
			Cal	Qtz+Fsp	Cly+OM	
TS2-perp	Perpendicular	1× (20×20)	65	11	19	5
TS2-para	Parallel	4× (10×10)				
TS4-para	Parallel	4× (10×10)	67	13	71	3

Cal = Calcite, Qtz+Fsp = Total quartz and feldspar. Cly+OM = Total clay minerals and organic matter

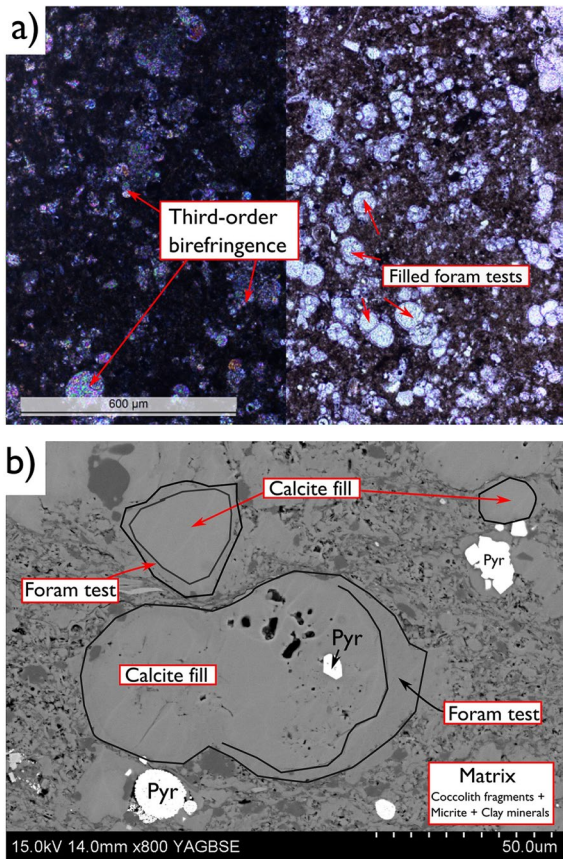

Fig. 2 **a** Optical microscopy image of TS2 taken under plane-polarised (right) and crossed-polarised light (left), and **b** back-scattered scanning electron microscopy (BSEM) image of the same sample. Pyr = pyrite

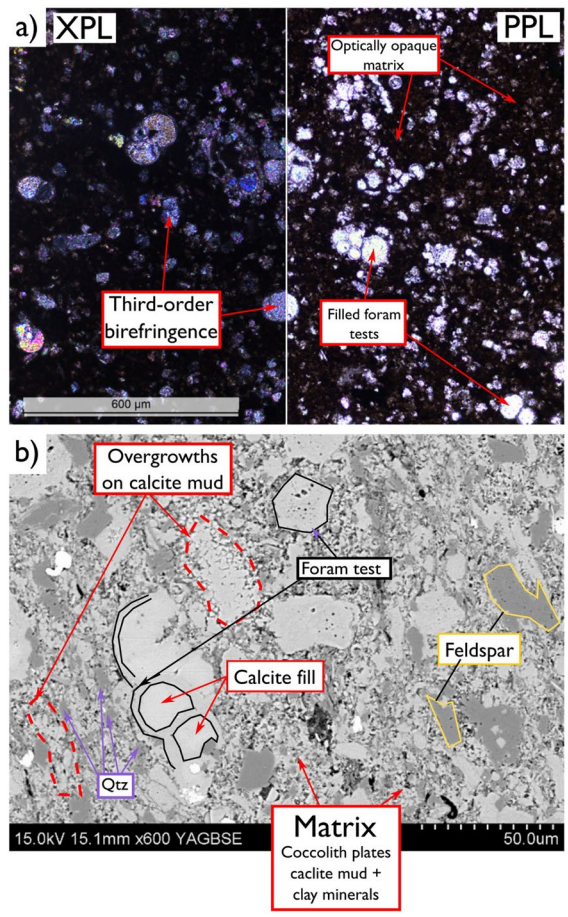

Fig. 3 **a** Optical microscopy image of TS4 taken under plane-polarised (PPL) and crossed-polarised light (XPLz), and **b** backscattered scanning electron microscopy (BSEM) image of the same sample. Qtz = quartz

in crossed-polarised light, again implying a mechanical continuity to the fills. Porosity is confined to the matrix. However, unlike the matrix of TS2, there are regions of TS4 where over-growths appear on grains of calcite mud (c.f. Figs. 2b and 3b). This leads to a "clotted texture", where the matrix porosity is locally reduced by calcite cements. The nanoindentation experiments presented in Sect. 3.2 aim to investigate if the diagenetic features discussed have a bearing on the elastic behaviour.

3.2 Micromechanical experiments

In this section we present the results of nanoindentation characterisation of the two samples whose microstructure was assessed in Sect. 3.1, and interpret the indentation results in terms of microstructure. Sample TS2 was mechanically characterised in both parallel and perpendicular directions, whereas TS4 was only characterised in the perpendicular direction. X-ray difraction (XRD) mineralogy and total organic carbon (TOC) analyses are also presented in to aid interpretation.

TS2: Bulk XRD analysis of the sample found a composition that is 65 vol% calcite, 19 vol% (Cly + TOC), and 11 vol% Quartz+Feldspar. Mercury injection (Hg-) porosimetry found 5 vol% pore space. Deconvolution of the mechanical data was performed according to he method of Ulm et al. (2007). In both the parallel and perpendicular directions, three mechanical phases could be resolved from the nanoindentation tests.

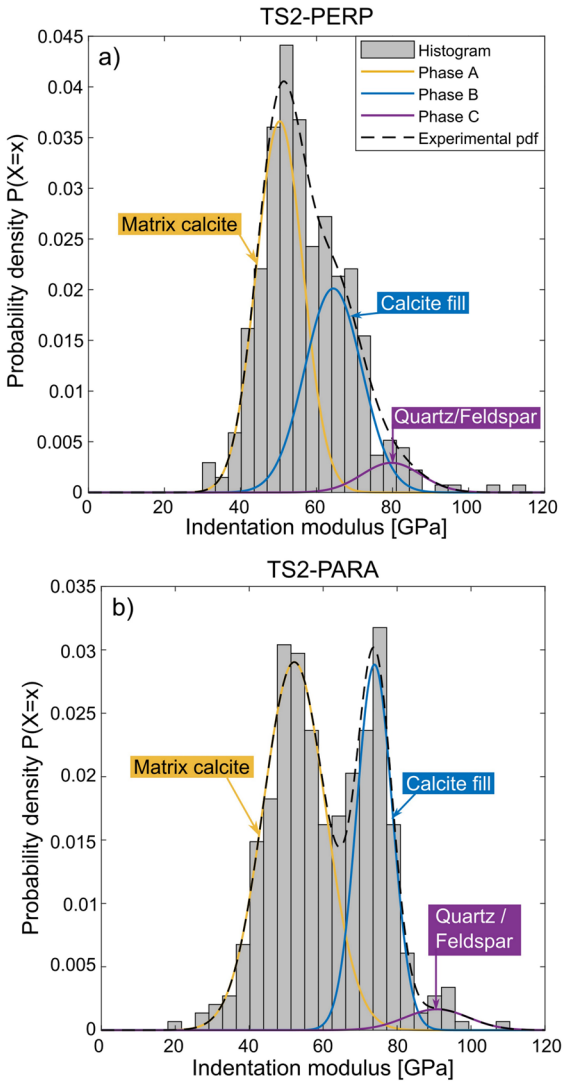

Fig. 4 Low-load nanoindentation data for sample TS2, in **a** the perpendicular and **b** parallel direction. Coloured curves correspond to deconvolution results (see text for details). The legend for (**a**) also applies to (**b**). The dashed line represents the theoretical probability density function representing the sum of deconvolution phases

The corresponding fractions, f, and indentation moduli, M, for TS2-Perp are: Phase A, $f = 0.56$ ($M = 50.3$ GPa ± 6.1), Phase B, $f = 0.38$ ($M = 67.4$ GPa ± 7.5) and Phase C, $f = 0.05$ ($M = 79.7$ GPa ± 7.7) (see Fig. 4a)).

For TS2-Para deconvolution yields: Phase A, $f = 0.62$ ($M = 52.2$ GPa $\pm$ 6.1), Phase B, $f = 0.34$ ($M = 73.9$ GPa $\pm$ 4.8) and Phase C, $f = 0.04$ ($M = 90.7$ GPa ± 8.6) (see Fig. 4b)).

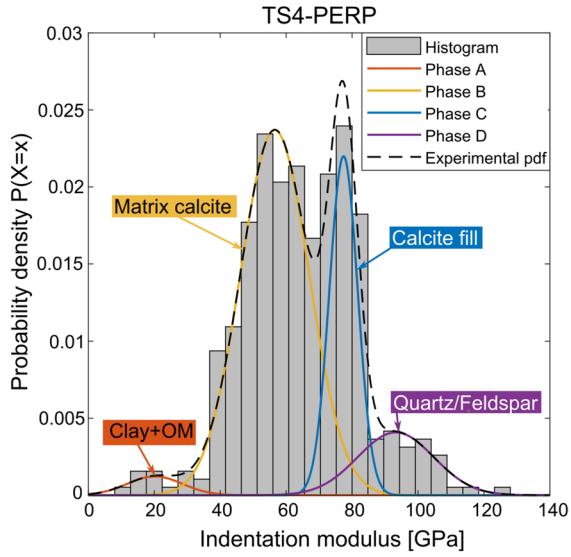

Fig. 5 Low-load nanoindentation for TS4 in the perpendicular direction. Coloured curves correspond to deconvolution results (see text for details). The dashed line represents the theoretical probability density function representing the sum of deconvolution phases. The theoretical pdf predicts slightly higher frequencies than the deconconvolution peak for phase C. This is due to the large tail in the distribution for phase D. This implies a greater degree of mechanical uniformity in the diagenetic calcite fill

TS4: Bulk XRD analysis of the sample find a composition that is 67 vol% calcite 17 vol% (Cly + TOC) and 13 vol% Quartz+feldspar. Hg-porosimetry found porosity to be 3 vol%. Deconvolution of the indentation modulus data returns finds four mechanical phases can be resolved (Fig. 5). The corresponding fractions and indentation moduli are as follows: Phase A $f = 0.03$ ($M = 20.3$ GPa ± 8.4) GPa. Phase B, $f = 0.62$ ($M = 56.6$ GPa ± 10.4), Phase C $f = 0.24$ ($M = 77.4$ GPa $\pm$ 4.3) and Phase D, $f = 0.11$ ($M = 92.8$ GPa $\pm$ 11.6).

3.3 Discussion of micromechanical results

In both samples, there is some disagreement between the clay-mineral and organic matter content as reported by XRD and TOC analyses, and deconvolution of the mechanical data. Since XRD is a bulk analysis technique, it does not necessarily reflect the mechanical role a given mineral plays microstructurally. Graham et al. (2021) suggested that mudstone nanoindentation data is best interpreted in terms of

mechanically active phases rather than mineralogical ones. Also, grid indentation is essentially a 2D analysis technique concerned with areal fractions rather than volume fractions, since the spatial extent of the grid is far greater than the depth dimension sampled. Therefore, a perfect agreement with deconvolution should not necessarily be expected, particularly since clay minerals are well mixed with one another, and within the clay-sized calcite in the matrix of the samples (Fig. 2b).

For both parallel and perpendicular tests on TS2, the softest indents on Phase A are likely related to indents that sample a composite of calcite, clay minerals and organic matter in the interparticle interstices. The same argument is made for the softest indents in Phase B in sample TS4, this interpretation is in good agreement with earlier work considering the elasticity of the Eagle Ford matrix (Graham et al. 2021, their Table 4)

The fraction associated with Phase D in Fig. 5 is in good agreement with XRD data, supporting an interpretation of it being related to the quartzofeldspathic response. The same is true of the stiff tail of phase B in both samples from TS2. The measured indentation moduli for the quartzofeldspathic phases in both samples yield stiffer indentation moduli than measured by AFM by Graham et al. (2021) elsewhere in the Eagle Ford ($M \sim 56$ GPa). However, in that study, we did not specifically consider diagenetic influences in the interpretation. Milliken et al. (2016) suggested that up to 85% of quartz present in the Eagle Ford is likely diagenetic, formed from a dissolution-reprecipitation mechanism. They suggested that in order for euhedral crystals to form, then this must form early earlier in the burial history, at depths between 1–2 km. Porosity at such depths are high enough, and pores are large enough to allow for authigenic quartz to grow into crystals that better approximate ideal crystal geometries. Our measured peaks at $M = 90.7$ GPa and $M = 92.8$ GPa would suggest that in TS2-Para and TS4, that diagenetic processes lead to "expected" elasticity in the quartz fraction. Orientation effects may be at play to explain the slightly lower value of $M = 79.7$ GPa in TS2-Perp.

The non-calcite indents have now been accounted for. A common feature to all three samples is a bimodal distribution to the remaining indentation data corresponding to calcite (Figs. 4a, 4b and 5), with major peaks at $\sim$ 50 GPa and $\sim$ 70 GPa (c.f Graham et al. 2021, their Fig. 9). This is now discussed.

Optical microscopy conducted showed uniform extinction of calcite fills during rotation of the sample stage under crossed-polarised light. This implies that the calcite fills grew in optical continuity throughout their growth history, and can be considered mechanically as single crystals. From a size perspective, they crystals filling tests are up to 75 μm on their long axis (Fig. 2). The crystals filling the tests are therefore much more morphologically similar to the ideal crystals of Iceland-spar calcite usually measured for elastic properties incorporated in literature data tables (Chen et al. 2001; Mavko et al. 2009). This contrasts with the calcite debris in the matrix at up to 5 μm in size with much less well defined crystallinity. In the subsequent discussion, we take crystallinity to describe how close to an ideal calcite crystal (e.g Chen et al. (2001)) particular material is.

Mavko et al. (2009) provide bulk and shear moduli for ideal calcite as K = 76.8 GPa, G = 32 GPa, respectively. This corresponds to E = 84.3 GPa and $\nu = 0.31$. The equivalent isotropic indentation behaviour using Eq. 1b is $M^{ISO} = 94$ GPa. Whilst for TS2 and TS4, the stiffest indents for calcite on average are 73–77 GPa, and some 20 GPa lower than estimates from Mavko et al. (2009). The lower values measured here may in part be due to deviations from ideal crystal geometry imposed by the constraints of the spheroidal chambers in which the calcite grew. The comparison of our data to M^{ISO}=94 GPa is based on the regularity with which data from Mavko et al. (2009) is cited in micromechanics studies. It is worth noting that highly crystalline calcite measured by Broz et al. (2006) was reported at 78.1 GPa for an indentation vector perpendicular to the crystallographic c-axis. This is much closer to our experiments, and the crystalline, organic-poor sample of Eagle Ford mudstone considered by Mashhadian et al. (2018b). In conclusion, a more direct comparison between indentation moduli measured in our samples and the Young's modulus of ideal calcite can be made in the case of foraminifera fills. Next, the matrix calcite is shown to be mechanically distinct from that of the foraminifera fills.

Previous work on the Eagle Ford by Mashhadian et al. (2018b, their Table 3) has recorded low indentation moduli between $M = 34$ GPa and $M = 46$ GPa for organic rich samples similar to those in this study. They suggested that these low values (compared to $M \sim 70$ GPa for their "organic-poor" samples) are due to the influence of organic matter at the scale of the indenter. We can test this hypothesis through application of a mean-field homogenisation model. The Self-Consistent scheme (Eq. 2a & 2b) is a common model used to consider the effective elastic properties of clay-sized material well-mixed with organic matter in both clay mineral and carbonate rich mudstones (e.g. Ortega et al. 2007, Charlton et al. 2021).

Figure 6 shows the predicted indentation moduli for a mixture of calcite and organic matter, modelled using the Self-Consistent scheme. In order to produce indentation moduli in range found in the matrix of TS2 and TS4 (yellow deconvolution peak in Figs. 4 and 5), the sample needs to contain between 20% and 45% organics at the scale of the low-load indentation test (Fig. 6). For samples TS2 and TS4, we have ~ 65 vol% calcite from XRD, and TOC of ~ 3 vol%. This corresponds to only around 4 vol% in a mixture of calcite and organic matter alone (as in the matrix). From Fig. 6, this is not enough to explain the low reported indentation moduli by mixing alone. Furthermore, in our calculations base the crystalline calcite end-member not only on literature derived calcite values (Mavko et al. 2009), but also on indentation-based experimental data (upper and lower red curve respectively). Additionally, we use full the full range of known Eagle Ford organic matter elasticity (Fender et al. 2020a) to account for uncertainties in this parameter over the wider formation. Accounting for these uncertainties, the same conclusion is reached; the samples are too poor in organic matter for this alone to explain the softer matrix response. Therefore, we must conclude that the calcite in the matrix of TS2 and TS4 is itself intrinsically less stiff than that filling the foraminifera tests. Figure 7 shows a map of one of the four indent grids conducted on sample TS2-Para, not that the two distinct mechanical domains.

It should be noted that the Eagle Ford samples considered by Mashhadian et al. (2018b) are thermally immature outcrop examples. Outcrop Eagle Ford samples considered by Gaiani (2020) correspond to T_{max} of ~435 °C (vitrinite reflectance 0.4%R_0). The strike of Eagle Ford outcrop is generally regionally parallel to the maturity contours (Mullen 2010). This contrasts with the gas window maturity of our samples.

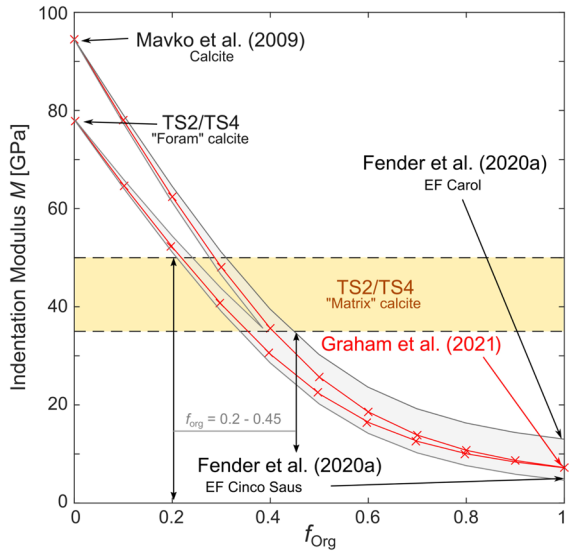

Fig. 6 Predicted indentation moduli (Eqn. 3c) for the clay-sized matrix modelled as a granular mixture of organic-rich calcite using the Self-Consistent scheme. The indentation modulus is presented as function of the fraction of organic matter in the mixture, f_{Org}. The upper red line uses a crystalline calcite end-member taken from Mavko et al. (2009), corresponding to the most common literature-based assumption. The lower red line corresponds a indentation-based crystalline calcite end-member equivalent to our experimental results for foraminifera-filling calcite. The organic matter end-member is taken from atomic force-microscopy measurements published by Graham et al. (2021) on samples from the same well as TS2 and TS4. To account for variability in organic matter elasticity within the wider formation, the red curves are bounded by values from Fender et al. (2020a) for other Eagle Ford wells (Carol and Cinco Saus)

Whilst broadly similar results can be inferred between Mashhadian et al's (2018b) work and the current study, two points should be emphasised. Firstly, that we note two distinct mechanical behaviours for calcite are seen in a single sample, implying that such mechanical nuances can be resolved by indentation tests and examined using simple microstructural models. Secondly, the elastic response of *both* crystalline calcite and matrix calcite in Mashhadian et al's samples is softer than ours by ~ 10 GPa (which is on the order of one standard deviation of the deconvolution results presented in Sect. 3.2). This

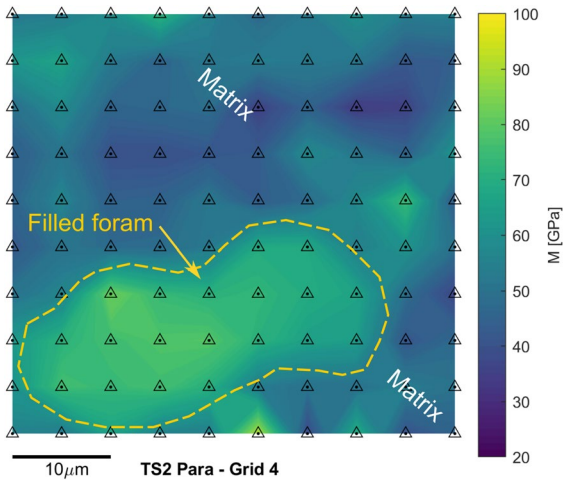

Fig. 7 Indentation modulus, M, map for TS2-Para, (grid 4). Note the distinction between two mechanical domains (compare to Fig. 4a). The region of stiffer indentation response is morphologically similar to the foraminifera tests seen in Fig. 2. Triangle symbols show positions of indents

suggests that burial history may play a role in the observed *intrinsic* stiffness of calcite. This is investigated further in Sect. 4.

3.4 Integration with existing datasets

Graham et al. (2022) conducted micromechanical modelling of Eagle Ford samples from the same well as TS2 and TS4. Although the low-load indentation data presented here was not available in that work, it was found both numerically and experimentally that the calcite in the matrix actively contributes to the transverse anisotropic behaviour of the bulk sample. This is not unique to the Eagle Ford. Active contributions from calcite to the anisotropic behaviour of the clay-sized matrix of the Evie formation of the Horn River shale was observed experimentally by Charlton et al. (2023). The modelled elastic constants for calcite from that work are presented in Table 2, alongside equivalent constants on highly crystalline material from Chen et al. (2001). The experimentally derived low-load indentation moduli for the calibration and validation datasets considered by Graham et al. (2022) revealed that $M_1/M_3 \sim 1.11$ describes the calcite matrix. Including the indentation moduli for *matrix* calcite for TS2 and TS4 from this study into the existing dataset only slightly alters that value

Table 2 Transverse isotropic elastic constants for calcite. Note that Chen et al. (2001) is from experiments on crystals

C_{ij} (GPa)	C_{11}	C_{12}	C_{13}	C_{33}	C_{44}
Graham et al. (2022)	57.5	13.4	3.0	39.7	34.1
Chen et al. (2001)	149.4	57.9	53.5	85.2	34.1

Graham et al. (2022) is from calibration of a micromechanical model constrained by low- and high-load nanoindentation data at the scale of the carbonate-rich matrix, and the mudstone composite.

to $M_1/M_3 \sim 1.15$. This demonstrates the experimental fidelity of the current work, and further strengthens our existing hypothesis that in calcareous mudstones, clay minerals cannot be assumed to be the sole source of anisotropy (c.f. Ortega et al. (2007)). In our experiments the large-scale isotropy of calcite in the foraminifera fills was not conclusively resolved since we only able to undertake measurements on three samples. However, the organic-poor sample from Mashhadian et al. (2018b) displays little anisotropy in the indentation modulus. It is therefore likely that at the scale of the bulk shale composite, the net behaviour of calcite fill is isotropic. This assumption was made in the calculations underpinning Fig. 6.

4 Inverse micromechanical modelling

In Sect. 3.3, we hypothesised that the softer indentation moduli in the outcrop samples may be related to their lower thermal maturity than the gas window samples. Gordin et al. (2016) and Shitrit et al. (2019) provide mechanical characterisation of a set of thermally-immature and shallowly buried, organic-rich chalks from the Ghareb and Mishash formations of Israel. The organic-rich chalks were chosen as they are a closely related class of fine-grained rock. These are compositionally simpler than the Eagle Ford examples, comprising largely calcite and organic matter. This makes the inverse analysis straightforward and minimises the possibility of non-calcite mineral phases playing a significant role in influencing the results. Additionally, these particular examples are thermally immature, with a reported Rock Eval T_{max} of 412 °C (Shitrit et al. 2019), and have experienced only modest burial (Burg and Gersman 2016). The starting point for our inverse analysis are

the elastic constants provided in Gordin et al. (2016, their Table 1), and Shitrit et al. (2019, their Table 4); porosity and organic content is also taken from those references.

4.1 Selecting appropriate organic matter properties

Using the experimental data of Gordin et al. (2016) and Shitrit et al. (2019), we perform inverse micromechanical analyses in order to solve for the required elastic constants of calcite. Inverse analysis in terms of calcite is feasible owing to advances in our understanding of the diagenetic evolution of the elasticity of organic matter. This has been achieved through numerous atomic force microscopy studies of amorphous organic matter (Eliyahu et al. 2015; Emmanuel et al. 2016; Goodarzi et al. 2017; Fender et al. 2020a), and AFM and nanoindentation studies of coal macerals (Vranjes et al. 2018; Fender et al. 2020b).

Particularly, the work of Fender et al. (2020a) provides a comprehensive experimental dataset of organic matter elasticity in a wide range of mudstones (Barnet, Eagle Ford, Tarfaya, and Bowland) covering the spectrum of both organic matter *type* (Type II and III, predominantly amorphous organic matter) and *maturity* (Immature Tarfaya, early and late oil window examples from the Barnett and Eagle Ford, and gas window Bowland samples). Immature type I kerogen from the Green River formation was additionally considered by Fender (2020). With the exception of the Green river examples, a bimodal distribution in Young's modulus of OM is observed. In contrast to the work of Eliyahu et al. (2015), Fender's work considers organic matter as a matrix-wide component, rather than as isolated grains.

The kerogen in the Ghareb formation is type II-S (Shitrit et al. 2019), and reported values of T_{max} are comparable to the Tarfaya samples from Fender et al. (2020a). Therefore, we use Young's modulus for the aliphatic peak in the modulus distribution of the Tarfaya mudstone for our modelling ($M = 6.8$ GPa, and a Poissons ratio of $\nu = 0.27$ is assumed. Fender et al. (2020a) demonstrated that sample-wide heterogeneity in terms of M in organic matter is greater than the degree of uncertainty imparted by assuming a value of ν. Similar Poisson's ratios are obtained on coal samples (Morcote et al. 2010)).

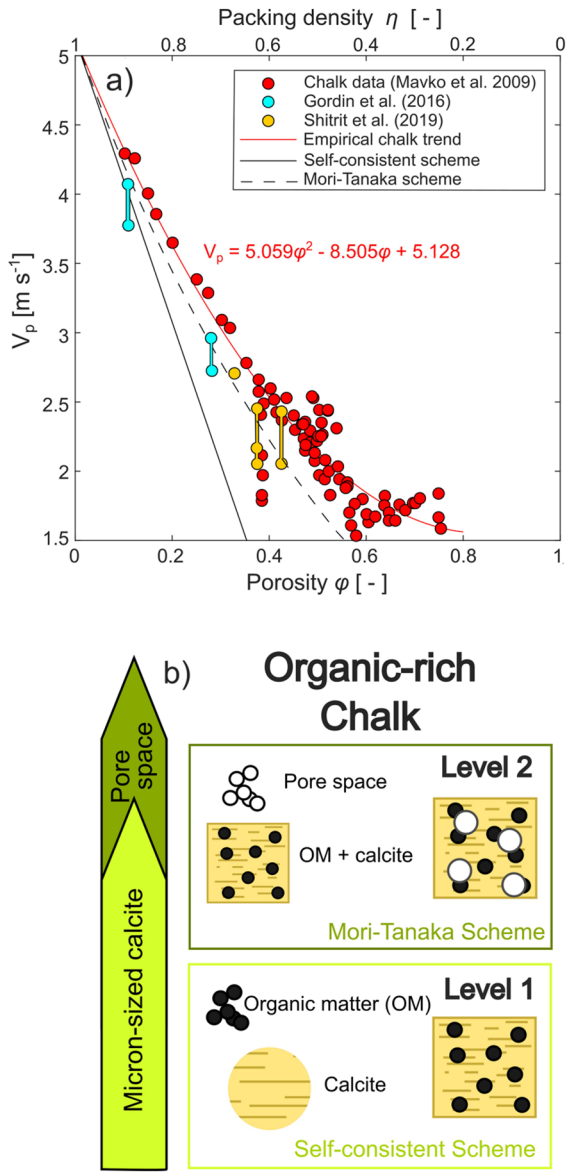

Fig. 8 **a** $V_p - \phi$ relationship for chalks adapted from Mavko et al. (2009, their Fig. A.1.2) along with predicted trends assuming Self-Consistent and Mori–Tanaka micromechanics. Overlain are the experimental results of Gordin et al. (2016) and Shitrit et al. (2019). Note that the high porosity samples in a) from Mavko et al. (2009) are water-saturated. This will change the *absolute* velocity, but does not alter the illustrative purpose of the figure that a model that can support non-zero velocities at porosities above 0.5 is needed for chalks. **b** Two step micromechanical model used in Sect. 4.3 to calculate bulk chalk elastic properties

4.2 Conceptual model

In order to keep the interpretation of the results of Gordin et al. (2016) and Shitrit et al. (2019) as consistent as possible with our Eagle Ford experiments, and other micromechanical studies (Ortega et al. 2007; Goodarzi et al. 2016; Li et al. 2019; Charlton et al. 2021), we pose our inverse analysis in a mean-field homogenisation framework (see Sect. 2.2).

In clay mineral-rich mudstones, the Self-Consistent scheme is often used to model granular porous materials, owing to its percolation threshold being close to that of packed spheres (Bobko and Ulm 2008). Figure 8a shows P-wave velocity (V_P) data for chalks compiled by Mavko et al. (2009), alongside the $V_P - \phi$ scaling line expected under the Self-Consistent and Mori–Tanaka schemes. It is clear that the matrix-pore interaction in chalks is better described under a Mori–Tanaka type micromechanics, this model is employed in following work. The Self-Consistent scheme remains valid for modelling the effective properties of the calcite-organic matter skeleton, which we consider a granular mixture.

4.3 Inverse formulation

A two step process is used to back-calculate the elastic contribution of calcite (Fig. 8b). A first stage calculation is performed to estimate the elastic properties of the rock skeleton by removing pore space. Secondly, a calculation is performed to determine the elastic constants of calcite required to give the results of stage one when mixed with organic matter in correct proportions. This is illustrated in Fig. 9. To enable the first step of the inversion numerically, the general expression for calculating the elastic constants of the solid matrix of of a porous material is employed (Eq. 4a – see Chateau and Dormieux (2002) for a derivation). For step two, a forward model (Eq. 4b—note that this is a specific case of Eq. 2a) for a two-phase granular mixture of calcite and organic matter is iteratively evaluated varying $\mathbb{C}_{\text{Cal}}$. For each iteration of Eq. 4b, the solution is compared against the solution to 4a obtained from the core-scale tests. The matrix calcite constants, $\mathbb{C}_{\text{Cal}}$, are obtained by minimising the L2-norm between the two solutions (Eq. 4c)

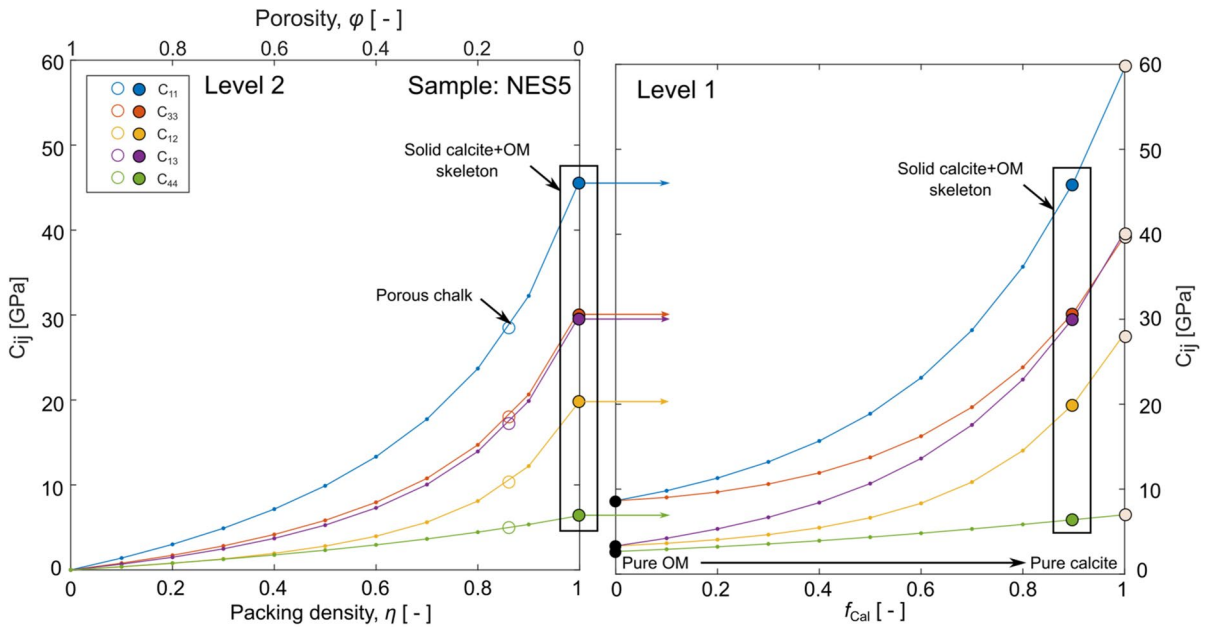

Fig. 9 Illustration of the inverse modelling approach outlined in Sect. 4.3 for sample NES5 in Table 3. For explanation of Level 1 and Level 2, see Fig. 8b

$$\mathbb{C}^{\text{Solid}} = \left(1 - \phi \mathbb{A}_{\phi}\right)^{-1} : \mathbb{C}^{\text{Hom}} \tag{4a}$$

$$\text{where } \mathbb{C}^{\text{Solid}} = f_{\text{OM}} \mathbb{C}_{\text{OM}} : \left[\mathbb{I} + \mathbb{P}^{\text{Solid}}_{\text{OM}} : (\mathbb{C}_{\text{OM}} - \mathbb{C}^{\text{Solid}})\right]^{-1} + \cdots \\ \cdots + (1 - f_{\text{OM}}) : \mathbb{C}_{\text{Cal}} \left[\mathbb{I} + \mathbb{P}^{\text{Solid}}_{\text{Cal}} : (\mathbb{C}_{\text{Cal}} - \mathbb{C}^{\text{Solid}})\right]^{-1} \tag{4b}$$

$$\min_{C^{\text{Cal}}_{ij}} \| \mathbb{C}^{\text{Solid}}_{\text{Eq. 4a}} - \mathbb{C}^{\text{Solid}}_{\text{Eq. 4b}} \|_2 \tag{4c}$$

In Eq. 4a, $\mathbb{A}_{\phi}$ is the interaction tensor between the pore space and the solid skeleton. The interaction tensor can be derived from first-priciples physics for both the MT and SC schemes, and represents the physical continuity of stress at the boundary of a pore or inclusion during the mapping macroscopic strains on the composite material to the local strains in the grain (Eshelby 1957; Hill 1965; Chateau and Dormieux 2002). As the V_P-porosity relationship for chalks follows a MT model, $\mathbb{A}_{\phi}$ is given by Eq. 3b.

The sequence of calculations contained within equation 4c for the constants of the calcite matrix is justified since $\mathbb{C}^{\text{Hom}}$ is known from core-scale tests, with the elastic constants of the organic matter known from micromechanical experiments in terms of M^{ISO} (Eq. 1b, also refer back to Sect. 4.1 for justification on converion in terms of E and ν. In this work E and ν were transformed into components of the compliance tensor $\mathbb{S} \equiv \mathbb{C}^{-1}$) through standard relationships for linear elasticity (Mavko et al. 2009, pg. 35). $\mathbb{C}_{\text{OM}}$ is then obtained as the matrix inverse of $\mathbb{S}_{\text{OM}}$. In any micromechanics model, the observation-based conceptual model used to choose the micromechanics scheme is key, but is still an idealisation. In this particular case, the samples are mainly composed of calcite, therefore we do not expect the inversion to be particularly sensitive to geometric simplifications made during conceptual modelling when solving for the dominant mechanical phase.

4.4 Modelling results and discussion

The transverse isotropic elastic constants corresponding to calcite in the samples of Gordin et al. (2016) and Shitrit et al. (2019) are provided in Tables 3 and 4. In order to compare the behaviour of these samples to the experimental results of Sect. 3.2, and literature data, the corresponding transverse isotropic indentation moduli are calculated according to Eqns. 1c and 1d (Delafargue and Ulm 2004).

Table 3 Inverse modelling of elastic constants for matrix calcite using data from Gordin et al. (2016)

	Samples			Mean
	Zoharim	NES5	NES3	
Tmax (°C)	410*	429*	428*	
Elastic constants C_{ij} (GPa)				
C_{11}	28.2	59.6	29.1	38.9
C_{12}	10.3	28.3	17.8	18.1
C_{13}	12.6	40.3	13.9	22.3
C_{33}	24.8	39.8	20.4	28.3
C_{44}	6.3	7.0	5.6	6.3
Predicted indentation moduli (GPa)				
M_1	22.3	31.3	18.3	24.0
M_3	19.1	17.4	15.5	17.3
M_1/M_3	1.17	1.80	1.17	1.38

*T_{max} data from Gordin et al. (2020) are given for context

Table 4 Inverse modelling of elastic constants for the calcite matrix using data from Shitrit et al. (2019)

	Samples				
	332.5	431.5	457.5	540	Mean
Elastic constant C_{ij} (GPa)					
C_{11}	28.8	28.0	27.3	49.8	33.3
C_{12}	9.5	13.7	11.4	29.1	15.9
C_{13}	1.9	8.3	8.9	15.3	8.6
C_{33}	15.3	17.2	19.2	30.4	20.5
C_{44}	6.4	4.6	5.1	8.1	6.1
Predicted indentation moduli (GPa)					
M_1	23.6	19.8	20.7	32.6	24.2
M_3	15.8	14.4	15.9	25.3	17.9
M_1/M_3	1.49	1.37	1.30	1.29	1.36

T_{max} is 412 °C on average over all samples

It is seen from both Tables 3 and 4 that the elastic constants for the calcite matrix in the shallowly buried, anisotropic chalks are significantly lower than expected from Chen et al. (2001), and also from Graham et al. (2022) (see Table 2). Our inverse modelling results predict indentation moduli for the matrix of the samples of Gordin et al. (2016) and Shitrit et al. (2019) that are around 50% of those measured by indentation on matrix carbonate in TS2 and TS4 of this study in terms of M_1. The predicted M_3 indentation moduli for the chalk matrix are significantly

softer than TS2 and TS4, typically less than 20 GPa. We also note that they are also elastically softer than those measured on the immature Eagle Ford samples. The predicted indention anisotropy of the chalks is also much more pronounced than that observed by Graham and Rouainia (2021) (M_1/M_3 ~1.15), with an average anisotropy of $M_1/M_3 \sim 1.37$ obtained from inverse modelling.

Viewing the inverse modelling results alongside the immature Eagle Ford data, as well as the new Eagle Ford data presented in Sect. 3 for thermally mature samples, it appears to that the calcite matrix of thermally immature and/or less thermally mature chalks (Tmax $\sim$ 410 °C) is intrinsically soft. We suggest that increased burial through the same temperature and pressure regimes that promote thermal maturation in the organic matter results in an elastic signature of fine-grained calcite that becomes increasingly stiff as in TS2 and TS4. The same process appears to also result in a loss in anisotropy. Dissolution-reprecipitation processes that lead to crystallisation of calcite either in void spaces (as in the case of the foraminifera chambers), or more extensive re-crystallisation of the sample, as in some regions of TS4 (Fig. 10). This leads to elastic responses more in line with those presented in Chen et al. (2001) and Mavko et al. (2009), where crystal geometry can be considered "ideal". Indeed such results are similar to those obtained by Wang (2002) on low porosity, coarsely crystalline limestones. The contribution of calcite to sample anisotropy appears to decrease, with increasing recrystallisation, with such regions behaving isotropically (as assumed in mean-field models by Ortega et al. (2007) and Charlton et al. (2021)).

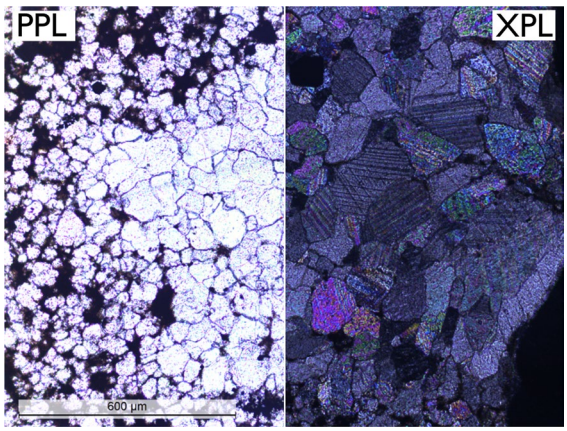

Fig. 10 Region of high crystallinity in sample TS4. This specific region was not targeted by the indentation tests, rather it illustrates a continuum of potential calcite morphology within a single Eagle Ford sample that has undergone intense local recrystallisation (see also Driskill et al. 2012)

5 Implications for future studies

Deriving micromechanically informed elastic properties that reflect diagenetic changes to calcite in calcareous sediments was the aim of this study, particularly properties that are presented in a mean-field homogenisation micromechanics framework. Additionally, we consider these results to represent micromechancially informed elasticities that capture diagenetic contributions without needing to invoke conceptually tenuous interfacial transition zones between phases (e.g Dubey et al. (2020)). Such zones are conceptually valid only if diagenesis is primarilly the result of cementitious overgrowths. Our results may simplify the procedure of incorporating cementation and recrystallisation effects, allowing a wider range of diagenetic and cementing mechanisms to be incorporated into in mean-field models without needing to significantly alter the numerical formulation. Our results are potentially useful input parameters for future studies employing mean-field homogenisation techniques to fine-grained carbonates. Based on the results of the previous sections, we present some illustrative examples of how our results can be applied within a mean-field homogenisation framework, these may be of use to future studies seeking benchmark values to interpret mechanical data in terms of diagenetic changes at the microscale.

5.1 Early burial and chemical compaction

Regarding the evolution of calcite elasticity during shallow burial, Fig. 11 illustrates predictions for the indentation moduli of soft anisotropic chalks as a function of porosity under the Mori–Tanaka scheme (c.f. Fig. 8) based on the predictions for "solid calcite" for samples from Gordin et al. (2016) and Shitrit et al. (2019). The predictions and approaches taken in Fig. 11 may provide a means of interpreting the elastic response for other chalk sequences comprising biogenic calcite that have undergone limited burial.

Here, mechanical compaction would be considered to dominate, prior to the onset of significant contact cementation or recrystallisation.

Grützner and Mienert (1999) consider the transition of calcareous ooze to chalk, with a region in their depth profiles where porosity remains essentially constant, yet P-wave velocity increases. Fabricius (2003) attribute the constant porosity to a lack of chemically enhanced compaction, with the associated P-wave behaviour attributed to contact cementation. Whilst this is in itself not controversial, cement volumes would need to remain small in order to reconcile the small changes to porosity, requiring that changes to the intrinsic stiffness of the grain also occur. The results from this study show a stiffening of the matrix beyond early burial. Samples TS2 and TS4 have matrix calcite stiffness of the same order of magnitude as stiffness reported by our earlier AFM work (Graham et al. 2021), where we were able to measure matrix calcite at the grain scale with nanometre resolution. Therefore, whilst cementation at grain contacts may contribute to stiffening of the overall framework, it may still be necessary to invoke changes to the intrinsic stiffness of the solid mineral skeleton (refer to Figs. 3b and 5. where cementitious overgrowths to matrix calcite are observed throughout the matrix, yet the mechanical signature remains distinct from the foraminifera fills), alongside purely mechanical porosity reduction.

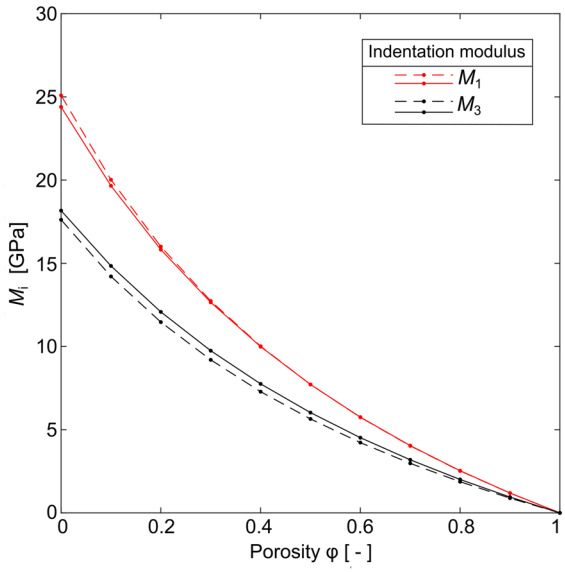

Fig. 11 Predicted indentation moduli for soft anisotropic chalk. Dashed lines use constants from Table 3, solid lines from Table 4

5.2 Calcite recrystallisation

Predictions (according to Eqn. 2a and 2b) for the indentation moduli of a hypothetical, calcareous sample that texturally lies between the matrix of TS2 and T24 (Table 2), and a fully re-crystallised example, in some regions of TS4 shown in Fig. 10 or the organic-free sample of Mashhadian et al. (2018b), are given in Fig. 12a. This relationship may be useful in understanding situations where pore-filling cement is present (as in the foraminifera tests) or the sample has undergone significant dissolution-precipitation recrystallisation. Figure 12a may be useful in the direct interpretation of higher-load nano- and microindentation tests. Alternatively, Fig. 6b presents the same mixing lines as Fig. 6a, but presented in terms of the individual elastic constants C_{ij}. This form may be more practical for interpreting ultrasonic velocity datasets in the same way.

For clarity, both Figs. 12a and b represent the zero-porosity mixing lines, corresponding to "solid-properties" of the mineral skeleton. Substitution of constants obtained from Fig. 12b into Eqns. 3a or 2a allow for the introduction of sample specific porosity. Porosity scaling relationships for transversely isotropic indentation moduli in terms of solid properties are given by Ulm et al. (2007, their Eqns. 12, 24a & b). It is expected that the results Fig. 12 are applicable to fine-grained carbonates that are at a more advanced stage of diagenesis, where porosities are low owing to chemically enhanced compaction beyond the limit of earlier mechanical compaction, or where dissolution-precipitation induced changes to texture are common. From Fig. 12b, the transition to a greater degree of crystallinity has a much smaller effect on the elastic shear constant C_{44}. The theoretical predictions offered in this section are based on the implicit assumption of burial under normal compaction conditions. Under such conditions it could be argued that normal compaction stiffening of the normal stiffness components (C_{11} and C_{33}) would be promoted due to active vertical loading, and passive earth pressure effects. The constant C_{13} is not related to a single deformation mode, rather being a function of the other four elastic constants Mavko et al. (2009). The mean-field

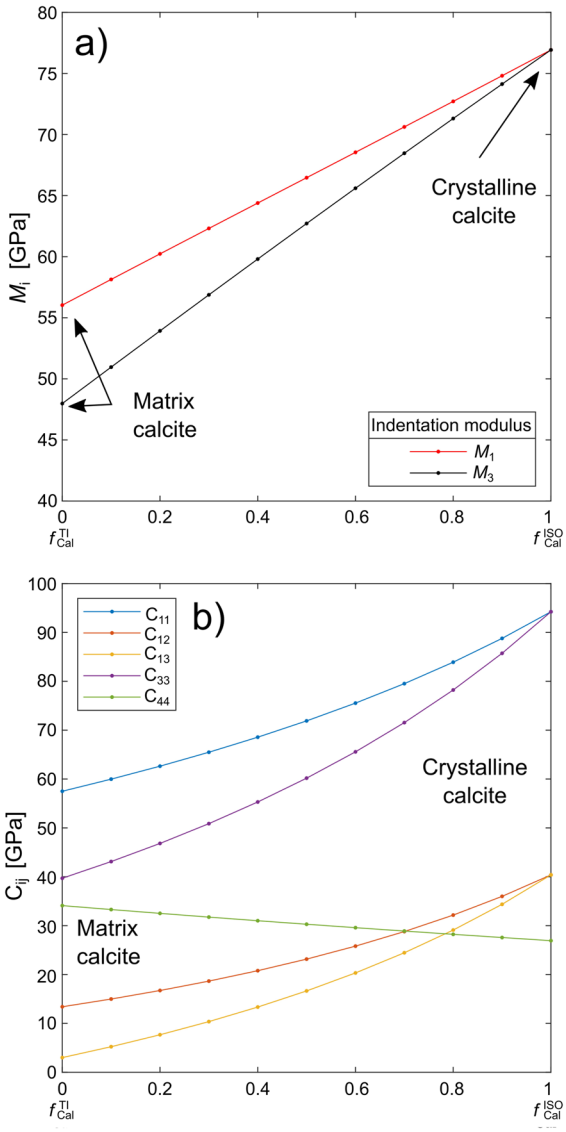

Fig. 12 **a** Predicted indentation moduli mixing lines for calcite end-members identified in TS2 and TS4. (see Table 2 for constants representing f^{TI}_{Cal}). **b** Same trends in terms of C_{ij}

schemes employed in this study are not designed to capture complex stress boundary conditions. It is conceivable that under more complex compaction scenarios, stress may promote a different evolution of C_{44} during burial. This may require more advanced 3D finite element simulations. Nevertheless, the parameters produced in this study may offer useful starting conditions.

5.3 Anisotropy

Calcite is intrinsically an anisotropic mineral (Chen et al. 2001), which may explain the observed transverse-isotropy noted in the Eagle Ford and Golan samples. However, a net anisotropic signature of the rock *fabric* would only be observed if there was some degree of alignment to the crystallographic $c-$axis. Although specific studies of $c-$axis alignment in undeformed carbonate sediments are few, Wenk et al. (2008) illustrate that they do occur. In their study of the Opalinus mudstone they found alignment of $c-$axes parallel to bedding, consistent with low-temperature compaction during early burial. However, Wenk et al. (1973) note that preferred crystallographic alignment in calcareous sediments is not ubiquitous (contrast this with the smectite-illite transformation). Whilst the examples considered in this paper show pronounced transverse-isotropy, it is clear from our results that re-crystallisation appears to promote an overall increase in isotropy. This may reflect a dissolution-reprecipitation-based diagenetic pathway, whereby crystallisation of calcite from solution may be locally influenced by an isotropic fluid pressure, rather than an anisotropic lithostatic stress field.

In light of the uncertainty surrounding preferred orientation in $c-$axis in carbonate sequences *generally*, it may be instructive to provide equivalent quasi-isotropic elastic constants derived from our experimental and modelling results. Isotropic values are convenient for application in more traditional rock-physics models based on Hashin-Shtrikman bounds (Fabricius 2003; Dvorkin and Alabbad 2019), (as these models do not account for anisotropy—which is a particular advantage of mean-field approaches). In order to do this, we compute the Voigt-Reuss-Hill (VRH) average for transversely isotropic materials (Antonangeli et al. 2005). This approach has been used successfully in mudstone studies (Ortega et al. 2007). A more advanced approach computing the closest isotropic elastic tensor is provided by den Boer (2014). The VRH bound of a given constant $[\bullet]_{VRH}$ is given by the arithmetic mean of the Voigt $[\bullet]_V$ and Reuss bounding values $[\bullet]_R$.

$$[\bullet]_{VRH} = \frac{1}{2}([\bullet]_V + [\bullet]_R) \tag{5}$$

where

$$K_V = \frac{1}{9}(2C_{11} + C_{33}) + \frac{2}{9}(C_{12} + 2C_{13}) \tag{6a}$$

$$G_V = \frac{1}{15}(2C_{11} + C_{33}) - \frac{1}{15}(C_{12} + 2C_{13}) + \frac{1}{5}(2C_{44} + C_{66}) \tag{6b}$$

$$K_R = \frac{1}{A(C_{11} + C_{12} + 2C_{33} - C_{13})} \tag{7a}$$

$$G_R = \frac{15}{2A(2(C_{11} + C_{12}) + 4C_{13} + C_{33}) + 6(1/C_{44} + 1/C_{66})}$$
$$\text{where } A = \frac{1}{C_{33}(C_{11} + C_{12}) - 2C_{13}^2} \tag{7b}$$

equivalent isotropic constants are given in Table 5. These calculations allow us to assess the effects of diagenesis on the other elastic constants. Up to now, the discussion has been based around the evolution of the indentation modulus, and by extension Young's modulus. The isotropic shear modulus of matrix calcite displays a consistent increase with burial, indicative of increased cementation bolstering the shear resistance. The bulk modulus of matrix calcite appears to show a less systematic evolution with burial, with $K_{\text{VRH}}^{\text{ISO}}$ remaining at ~ 20 GPa for the immature outcrop samples. Bulk modulus is a a measure of compressibility ($c_R = 1/K$), with the observation of a quasi-constant value of K in the matrix, further validating the approach of coupling indentation experiments with inverse micromechanical models for determining material properties at grain scale. This highlights the role of cementation in the observed stiffening of the samples at larger length scales. Furthermore, the observed stiffening in the indentation modulus values highlights that these are more sensitive to cementation effects than the bulk modulus, making indentation an attractive approach for quantifying the mechanical effects of diagenetic processes.

6 General discussion

We conclude by assessing how our results and hypotheses may fit within a wider understanding of how burial influences the elastic response of highly calcareous successions. Traditional macroscale studies consider the relationships between sonic velocity, V, as functions of porosity, ϕ. Micromechanics frameworks (see Fig. 1) set this on strong theoretical foundations, and relate them to the underlying microstructure. Mechanical compaction of a sedimentary sequence results in porosity loss, and thereby an increase in stiffness and sonic velocity. Normally, $V - \phi$ trends assume a constant *intrinsic* stiffness to the solid skeleton. Divergence from these trends implies a change in the intrinsic stiffness—as is seen

Table 5 Voigt-Reuss-Hill estimates of the equivalent isotropic properties of calcite for the studied samples

Samples	Equivalent isotropic constants [GPa]							
Samples	Tmax (°C)	$K_{\text{VRH}}^{\text{ISO}}$	$G_{\text{VRH}}^{\text{ISO}}$	$E_{\text{VRH}}^{\text{ISO}}$	$\nu_{\text{VRH}}^{\text{ISO}}$ [-]	$M_{\text{VRH}}^{\text{ISO}}$	Data	Notes
Matrix calcite								
Gordin et al. (2016)	410	25.5	7.03	19.3	0.37	22.3	See Table 3	Immature
Shitrit et al. (2019)	412	16.2	7.59	19.7	0.28	21.4	See Table 4	Immature
Mashhadian et al. (2018b)	428	*24.6*	*14.8*	*36.2*	0.29†	39.5	Their Table 3	Outcrop
Graham et al. (2022)	> 430	20.9	26.3	55.6	0.06	55.8	See Table 2	Gas window
Crystalline calcite								
Mashhadian et al. (2018b)	428	*47.5*	*21.7*	*55.9*	0.29†	61.1	Their Table 3	Outcrop
This study	> 430	*55.9*	*27.3*	*70.5*	0.29†	77.0	Sect. 3.2	Gas window
Chen et al. (2001)	N/A	76.1	36.3	93.9	0.29	102.5	See Table 2	Ideal crystal

Values in italics are calculated starting from indentation moduli and an assumed Poisson's ratio (marked with a dagger (†)) and taken from Chen et al. (2001). In these cases Young's modulus is determined first from Eq. 1b

during the smectite-illite transition in clay-rich mudstones (Goulty et al. 2016, their Fig 6).

Numerous studies have assessed the $V-\phi$ trends for carbonate rocks (Fabricius 2007; Brigaud et al. 2010; Regnet et al. 2015). However it is observed that the strength of such trends is a strong function of the host carbonate rock *texture*. Brigaud et al. (2010) note such a well-defined monotonic $V_P-\phi$ curves for calcareous mudstones and marls. However, their data for grainstones show considerable scatter. Grainstones are classically defined by Dunham (1962) as grain-supported carbonate sediments, with spar cements in the matrix. Brigaud et al. (2010) attribute this scatter to the diagenetic pathways taken by the sample. They suggest early cementation by blocky calcite cement promotes an increase in V_P by stiffening grain contacts, whilst maintaining a continuous, connected network in the remaining pore space. This contrasts with later cementation following early compaction, where cementation by blocky calcite occludes remaining porosity leading to a dense, fused microstructure. This conclusion would be better supported by two distinct $V_p-\phi$ trends. This is not supported by (Brigaud et al. 2010, their Fig. 8a), nor do they comment on the *details* of the grain composition (other than they are calcareous). For example, ooids are grains comprised of calcite mud. Lebedev et al. (2014) report the indentation moduli of ooids to be $M\sim 40-50$ GPa similar to the matrix in TS2 and TS4. An alternative interpretation of the scatter seen in their grainstone $V_P-\phi$ trend could be explained by contrasts in intrinsic elasticity between the grains and the cements, which would supported by observations made in this paper.

Dunham (1962) makes a sharp distinction between a mud matrix (packestone) and a crystalline one (grainstone). In reality a continuum is observed. Regnet et al. (2015) note a strong $V_P-\phi$ trend for fine-grained carbonates; however they also present their results grouped by micrite morphology. They found that fused and partially recrystallised micrite microstructures coincided with the stiffest samples and with the largest grain size. Parallels can be drawn from this study, crystalline fills display an intrinsic stiffness increase. This would suggest that the degree of matrix crystallisation impacts sonic response, and is supported by our data at varying diagenetic states.

The preceding discussion has highlighted how the results presented in this paper can potentially enhance the interpretation of $V-\phi$ relationships by providing better constrained end-member mechanical properties for rock-physics modes directly related to diagenetic observations. Fabricius (2003) accounts for diagenetic factors in a Hashin-Shtrikman framework (Mavko et al. 2009) by considering a mixture of calcite grains and water, as a function of porosity, where cementation is modelled by transferring solid from suspension and adding it to the load bearing framework. Our results may be able to supplement the model of Fabricius (2003) by introducing distinct elastic constants for the primary calcareous material, and stiffer constants for the crystalline material reflecting structural changes at the grain scale, as well as incorporating the influence of pore-filling and contact cements. Therefore, there is scope for micromechanical analyses to complement and enhance the interpretation of core-scale experiments in diagenetically and microstructurally complex carbonate rocks.

7 Conclusions

This paper has presented new micromechanical data for thermally mature, carbonate-rich mudstones from the Eagle Ford formation, demonstrating resolvable mechanical differences intrinsic to calcite between the soft anisotropic matrix ($M=40$-50 GPa) and diagenetic fills to forams ($M\sim 70$ GPa). These results have been compared against other Eagle Ford samples from the literature that are less thermally mature. The comparison suggested that burial processes may lead to intrinsic stiffening of calcareous constituents by ~ 10 GPa. Inverse modelling of organic-rich chalks also suggets that increasing burial promotes an increase in intrinsic stiffness, and a loss of anisotropy as samples recrystallise. The data presented in this paper is consistent with a mean-field homogenisation based micromechanics framework. Therefore, the data may be of use as a starting point for future work modelling calcareous rocks using these techniques, with data that reflects diagenetic subtleties. Additionally, these results have demonstrated that nanoindentation is a viable tool for exploring micromechanical effects related to diagenetic changes in microstructure.

This paper has demonstrated resolvable differences in the intrinsic stiffness of calcite in fine-grained sediment as a function of diagenetic state. The curves

presented in Figs. 12a and b, and 11 may act as reference points from which future indentation results obtained on highly calcareous samples can be interpreted without having to rely on the assumptions that calcite behaves as an ideal crystal (e.g. Mavko et al. (2009); Chen et al. (2001)). Since our data link mechanics to diagenetic state, it is hoped our data may provide alternative values with which to constrain other rock physics models (such as those based on Hashin-Shtrikman bounds) and allow for a more meaningful interpretation of velocity-porosity curves.

The specific reason for the lower in intrinsic stiffness of matrix calcite compared to crystalline cement has not been explored in this work. However, combining micromechanical experiments with SEM observations and detailed XRD analyses on calcareous rocks at various stages of diagenesis may shed light on this by linking micromechanics to mineralogical structure. The data presented in this paper may serve as a means to benchmark future mechanical results.

Acknowledgements Sam Graham was funded under an EPSRC CASE PhD studentship (Grant number EP5095281). Mohamed Rouainia and Andy Aplin were funded under NERC grants NE/R018057/1 and NE/R017840/1). Dr David Dewhurst of CSIRO is thanked for discussions during SG's PhD viva that greatly helped clarify some arguments to the benefit of the resulting manuscript. MicroMaterials ltd are thanked for fruitful discussions and technical assistance throughout the experimental work.

Author contributions All authors contributed to the study conceptualisation and completion. [Sam Graham] Primary data collection, analysis, and modelling. [Andrew Aplin, Mohamed Rouainia, Peter Armitage] contributed to funding acquisition and sample resourcing. [Sam Graham] prepared the original draft manuscript, all authors contributed to review and editing.

Data availability The data that support the findings presented in this paper are available from the corresponding author upon request.

Declarations

Conflict of interest The authors has no conflict of interest to declare that are relevant to the content of this article.

Consent to publish Not applicable.

Ethics approval Not applicable.

References

Abedi S, Slim M, Ulm FJ (2016) Nanomechanics of organic-rich shales: the role of thermal maturity and organic matter content on texture. Acta Geotech 11(4):775–787

Alnahwi A, Loucks RG, Ruppel SC et al (2018) Dip-related changes in stratigraphic architecture and associated sedimentological and geochemical variability in the Upper Cretaceous Eagle Ford Group in south Texas. AAPG Bull 102(12):2537–2568

Antonangeli D, Krisch M, Fiquet G et al (2005) Aggregate and single-crystalline elasticity of hcp cobalt at high pressure. Phys Rev B 72(13):134303

Bobko CP, Ulm FJ (2008) The nano-mechanical morphology of shale. Mech Mater 40(4–5):318–337

Brigaud B, Vincent B, Durlet C et al (2010) Acoustic properties of ancient shallow-marine carbonates: effects of depositional environments and diagenetic processes (Middle Jurassic, Paris Basin, France). J Sediment Res 80(9):791–807

Broz ME, Cook RF, Whitney DL (2006) Microhardness, toughness, and modulus of Mohs scale minerals. Am Mineral 91(1):135–142

Burg A, Gersman R (2016) Hydrogeology and geochemistry of low-permeability oil-shales- Case study from HaShfela sub-basin, Israel. J Hydrol 540:1105–1121

Charlton TS, Goodarzi M, Rouainia M et al (2021) Effect of diagenesis on geomechanical properties of organic-rich calcareous shale: a multiscale investigation. J Geophys Res 126:e2020JB021365

Charlton T, Rouainia M, Aplin A et al (2023) Nanoindentation of horn river basin shales: the micromechanical contrast between overburden and reservoir formations. J Geophys Res Solid Earth 128(3):e2022JB025,957

Chateau X, Dormieux L (2002) Micromechanics of saturated and unsaturated porous media. Int J Numer Anal Meth Geomech 26(8):831–844

Chen CC, Lin CC, Liu LG et al (2001) Elasticity of single-crystal calcite and rhodochrosite by brillouin spectroscopy. Am Mineral 86(11–12):1525–1529

den Boer LD (2014) An efficient algorithm for computing nearest medium approximations to an arbitrary anisotropic stiffness tensor computing nearest medium approximations. Geophysics 79(3):F1–F10

Delafargue A, Ulm FJ (2004) Explicit approximations of the indentation modulus of elastically orthotropic solids for conical indenters. Int J Sol Struct 41(26):7351–7360

Driskill B, Suurmeyer N, Rilling-Hall S et al (2012) Reservoir description of the subsurface eagle ford formation, Maverick Basin Area, South Texas, USA. In: SPE Europec/EAGE Annual Conference, OnePetro

Dubey V, Mashhadian M, Abedi S et al (2019) Multiscale poromechanical modeling of shales incorporating microcracks. Rock Mech Rock Eng 52(12):5099–5121

Dubey V, Abedi S, Noshadravan A (2020) Experimental characterization of microcrack-induced damage behavior in shale rocks using miniature tensile module. In: Proceedings of 54th US rock mechanics/geomechanics symposium, American Rock Mechanics Association, Golden, CO

Dunham RJ (1962) Classification of carbonate rocks according to depositional textures

Dvorkin J, Alabbad A (2019) Velocity-porosity-mineralogy trends in chalk and consolidated carbonate rocks. Geophys J Int 219(1):662–671

Eliyahu M, Emmanuel S, Day-Stirrat RJ et al (2015) Mechanical properties of organic matter in shales mapped at the nanometer scale. Mar Petrol Geol 59:294–304

Emmanuel S, Eliyahu M, Day-Stirrat RJ et al (2016) Impact of thermal maturation on nano-scale elastic properties of organic matter in shales. Mar Petrol Geol 70:175–184

Eshelby JD (1957) The determination of the elastic field of an ellipsoidal inclusion, and related problems. Proc R Soc London Ser A Math Phys Sci 241(1226):376–396

Fabricius IL (2003) How burial diagenesis of chalk sediments controls sonic velocity and porosity. AAPG Bull 87(11):1755–1778

Fabricius IL (2007) Chalk: composition, diagenesis and physical properties. Bull Geol Soc Den 55:97–128

Fabricius I, Røgen B, Gommesen L (2007) How depositional texture and diagenesis control petrophysical and elastic properties of samples from five north sea chalk fields. Petrol Geosci 13:81–95

Fender T (2020) Using atomic force microscopy to analyse the geomechanical properties of organic rich rocks. PhD thesis, Newcastle University

Fender T, Van Der Land C, Rouainia M et al (2020a) The assessment of organic matter young's modulus distribution with depositional environment and maturity. J Geophys Res 125(12):e2020JB020435

Fender TD, Rouainia CM, Van Der Land C, Jones M et al (2020b) Geomechanical properties of coal macerals; measurements applicable to modelling swelling of coal seams during CO2 sequestration. Int J Coal Geol 228(103):528

Gaiani I (2020) Controls on pore systems and surfaces of the carbonate-rich eagle ford formation. PhD thesis, Durham University

Goodarzi M, Rouainia M, Aplin AC (2016) Numerical evaluation of mean-field homogenisation methods for predicting shale elastic response. Comput Geosci 20(5):1109–1122

Goodarzi M, Rouainia M, Aplin AC et al (2017) Predicting the elastic response of organic-rich shale using nanoscale measurements and homogenisation methods. Geophys Prospect 65(6):1597–1614

Gordin Y, Hatzor YH, Vinegar HJ (2016) Ultrasonic velocity and anisotropy of organic-rich chalks. In: Proceedings 50th US rock mechanics/geomechanics symposium, American Rock Mechanics Association, Houston, TX

Gordin Y, Hatzor YH, Vinegar HJ (2020) Anisotropy evolution during early maturation of organic-rich carbonates. J Petrol Sci Eng 188(106):946

Goulty N, Sargent C, Andras P et al (2016) Compaction of diagenetically altered mudstones-part 1: mechanical and chemical contributions. Marine Petrol Geol 77:703–713

Graham SP, Rouainia M (2021) A revised conceptual model for calcareous shales: insights from mean-field homogenisation. In: Proceedings United Kingdom association of computational mechanics, Loughbourough

Graham S, Rouainia M, Aplin A et al (2022) New micromechanical data and modelling framework for the elastic response of calcareous mudstones. Int J Rock Mech Min Sci 158(105):181

Graham SP, Rouainia M, Aplin AC et al (2021) Geomechanical characterisation of organic-rich calcareous shale using AFM and nanoindentation. Rock Mech Rock Eng 54(1):303–320

Grützner J, Mienert J (1999) Physical property changes as a monitor of pelagic carbonate diagenesis: an empirically derived diagenetic model for Atlantic ocean basins. AAPG Bull 83(9):1485–1501

Guéry AAC, Cormery F, Shao JF et al (2010) A comparative micromechanical analysis of the effective properties of a geomaterial: Effect of mineralogical compositions. Comput Geotech 37(5):585–593

Hellmich C, Barthélémy JF, Dormieux L (2004) Mineral-collagen interactions in elasticity of bone ultrastructure-a continuum micromechanics approach. Eur J Mech A Solid 23(5):783–810

Herrmann J, Rybacki E, Sone H et al (2018) Deformation experiments on Bowland and Posidonia shale–Part I: Strength and Young's modulus at ambient and in situ p_c-T conditions. Rock Mech Rock Eng 51(12):3645–3666

Hill R (1965) A self-consistent mechanics of composite materials. J Mech Phys Sol 13(4):213–222

Laubach SE, Olson JE, Gross MR (2009) Mechanical and fracture stratigraphy. AAPG Bull 93(11):1413–1426

Laubach SE, Eichhubl P, Hilgers C et al (2010) Structural diagenesis. J Struct Geol 32(12):1866–1872

Lebedev M, Wilson ME, Mikhaltsevitch V (2014) An experimental study of solid matrix weakening in water-saturated savonnières limestone. Geophys Prospect 62(6):1253–1265

Li C, Ostadhassan M, Kong L et al (2019) Multi-scale assessment of mechanical properties of organic-rich shales: a coupled nanoindentation, deconvolution analysis, and homogenization method. J Pet Sci Eng 174:80–91

Mashhadian M, Abedi S, Noshadravan A (2018a) Probabilistic multiscale characterization and modelling of organic-rich shale poroelastic properties. Acta Geotech 13(4):781–800

Mashhadian M, Verde A, Sharma P et al (2018b) Assessing mechanical properties of organic matter in shales: results from coupled nanoindentation/SEM-EDX and micromechanical modeling. J Petrol Sci Eng 165:313–324

Mavko G, Mukerji T, Dvorkin J (2009) The rock physics handbook: Tools for seismic analysis of porous media, 2nd edn. Cambridge University Press

Milliken KL, Ergene SM, Ozkan A (2016) Quartz types, authigenic and detrital, in the Upper Cretaceous Eagle Ford Formation, south Texas, USA. Sediment Geol 339:273–288

Morcote A, Mavko G, Prasad M (2010) Dynamic elastic properties of coal. Geophysics 75(6):E227–E234

Mori T, Tanaka K (1973) Average stress in matrix and average elastic energy of materials with misfitting inclusions. Acta Metal 21(5):571–574

Mullen J (2010) Petrophysical characterization of the eagle ford shale in south Texas. In: Canadian unconventional resources and international petroleum conference, OnePetro

Obradors-Prats J, Rouainia M, Aplin A et al (2019) A diagenesis model for geomechanical simulations: formulation and implications for pore pressure and development of geological structures. J Geophys Res 124(5):4452–4472

Oliver WC, Pharr GM (1992) An improved technique for determining hardness and elastic modulus using load and displacement sensing indentation experiments. J Mater Res 7(6):1564–1583

Ortega JA, Ulm FJ, Abousleiman Y (2007) The effect of the nanogranular nature of shale on their poroelastic behavior. Acta Geoteh 2(3):155–182

Pommer M, Milliken K (2015) Pore types and pore-size distributions across thermal maturity, Eagle Ford Formation, southern Texas. AAPG Bull 99(9):1713–1744

Regnet JB, Robion P, David C et al (2015) Acoustic and reservoir properties of microporous carbonate rocks: Implication of micrite particle size and morphology. J Geophys Res 120(2):790–811

Røgen B, Fabricius IL, Japsen P et al (2005) Ultrasonic velocities of north sea chalk samples: influence of porosity, fluid content and texture. Geophys Prospect 53(4):481–496

Rybacki E, Herrmann J, Wirth R et al (2017) Creep of Posidonia shale at elevated pressure and temperature. Rock Mech Rock Eng 50(12):3121–3140

Scholle PA (1977) Chalk diagenesis and its relation to petroleum exploration: Oil from chalks, a modern miracle? AAPG Bull 61(7):982–1009

Shitrit O, Hatzor YH, Feinstein S et al (2019) Static and dynamic elastic moduli of organic-rich chalk. Geophys Prospect 67(3):624–650

Sondergeld CH, Rai CS (2022) A guide to nanoindentation. Petrophysics 63(05):576–590

Ulm FJ, Delafargue A, Constantinides G (2005) Experimental microporomechanics. In: Applied micromechanics of porous materials. Springer, pp 207–288

Ulm FJ, Vandamme M, Bobko CP et al (2007) Statistical indentation techniques for hydrated nanocomposites: concrete, bone, and shale. J Am Ceram Soc 90(9):2677–2692

Vranjes S, Misch D, Schöberl T et al (2018) Nanoindentation study of macerals in coals from the Ukrainian donets basin. Adv Geosci 45:73–83

Wang Z (2002) Seismic anisotropy in sedimentary rocks, part 2: laboratory data. Geophysics 67(5):1423–1440

Wenk HR, Venkitasubramanyan CS, Baker DW et al (1973) Preferred orientation in experimentally deformed limestone. Contrib Mineral Petrol 38(2):81–114

Wenk HR, Voltolini M, Loon VLR et al (2008) Preferred orientations and anisotropy in shales: Callovo-Oxfordian shale (France) and Opalinus clay (Switzerland). Clay Clay Miner 56(3):285–306

Zimmerman R (2000) Coupling in poroelasticity and thermoelasticity. Int J Rock Mech Min Sci 37(1–2):79–87